The low velocity impact response of curvilinear-core sandwich structures

T. Boonkong [a,b,*], Y.O. Shen [c], Z.W. Guan [a], W.J. Cantwell [d]

[a] School of Engineering, University of Liverpool, Brownlow Street, Liverpool, L69 3GH, UK
[b] Department of Engineering, The Royal Thai Naval Dockyard, Royal Thai Navy, Bangkok, Thailand
[c] School of Aerospace Engineering and Applied Mechanics, Tongji University, Shanghai, China
[d] Aerospace Research and Innovation Center, Khalifa University of Science, Technology and Research (KUSTAR), P.O. Box 127788, Abu Dhabi, United Arab Emirates

ARTICLE INFO

ABSTRACT

The low velocity impact response of lightweight aluminium sandwich panels, based on a curvilinear aluminium alloy core, has been investigated to evaluate their energy-absorbing characteristics and to identify the associated failure mechanisms. Finite element models are then developed to predict the dynamic response of these lightweight structures. Here, an elasto-plastic model, capable of accounting for strain-hardening effects, material rate-dependence, as well as the relevant damage criteria, was employed to predict the dynamic response of the targets. The finite element models were then validated by comparing their predictions against the corresponding experimental results. Good agreement was obtained, indicating that the models are capable of predicting the dynamic behaviour of these all-metal sandwich structures under low velocity impact conditions.

Once the finite element model had been validated, it was used to assess the effect of varying key test parameters, such as the projectile diameter, the material properties of the metal substrate as well as the angle of obliquity on the impact response. Here, it has been shown that the perforation energy increases as the impact angle is increased and also as the projectile diameter increases. An investigation of seven different all-metal sandwich structures has shown that an aluminium alloy offers the highest specific perforation resistance under conditions of low velocity impact loading.

1. Introduction

Sandwich panels, consisting of thin skins bonded to a low density core material, are finding widespread use in a wide range of applications, such as lightweight marine structures, impact-resistant land-transportation panels and high-performance load-bearing aerospace structures. Traditionally, most sandwich panels are based on either a lightweight polymer foam or metal foam or a honeycomb core. When skins are bonded, the resulting structures offer exceptional specific strength-to-weight ratios and stiffness-to-weight ratios, buoyancy, dimensional stability, thermal and acoustical insulation characteristics. A number of research studies have focused on the properties of sandwich panels based on corrugated cores. Curvilinear corrugated-core sandwich structures offer superior mechanical properties and various types of such sandwich structure have been studied in detail [1–10].

Curvilinear corrugated-core sandwich design has been used in the production of boxes and cardboard since the late 1800s [11]. They have been widely used in the packaging industry as a result of their low weight, recyclability and low cost. In the past, attempts have been made to predict the load-carrying capacity of corrugated box structures, most notably by McKee et al. [12]. Talbi et al. [11] analysed the geometric and mechanical properties of corrugated board components. They also studied the behaviour of these corrugated structures when subjected to transverse shear and torsion. Allaoui et al. [13] noted that corrugated cardboard is very sensitive to atmospheric conditions. Shear buckling of the core of a corrugated paperboard structure was investigated by Isaksson and Gradin [14]. It was shown that the structural strength of the panel decreases rapidly below a critical thickness of fluting. Tian and Lu [15] studied the minimum weight of a corrugated panel based on fibre reinforced composites subjected to a uniform axial compressive load in order to design an optimal corrugated panel. Haj-Ali et al. [16] presented a refined nonlinear finite element approach for analysing corrugated fibreboards. In their work, the anisotropic and nonlinear material stress–strain behaviour of the corrugated structured was modelled. It was found that the proposed refined modelling approach was able to accurately predict the overall

* Corresponding author. School of Engineering, University of Liverpool, Brownlow Street, Liverpool, L69 3GH, UK. Tel.: +44 (0)151 794 5386; Fax: +44 (0)151 794 4703.
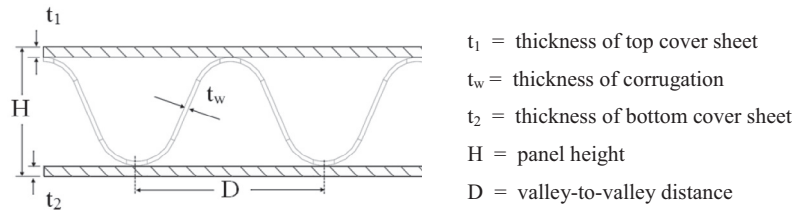E-mail address: t.boonkong@liv.ac.uk (T. Boonkong).

Fig. 1. Schematic of the cross-section of the curvilinear sandwich panel.

mechanical behaviour and ultimate failure in a wide range of corrugated systems.

Metallic corrugated core sandwich structures offer potential for use in a wide range of applications, such as those involving impact/ blast load mitigation. There is a limited amount of experimental and numerical data in the literature relating to the dynamic response of sandwich structures based on corrugated topologies. Rubino et al. [17] investigated the impact response of clamped stainless steel Y-framed and corrugated core sandwich plates loaded by aluminium foam projectiles. At low values of projectile momentum, the sandwich panels deflected less than their monolithic counterparts. However, at higher values of projectile momentum, the sandwich panels failed in a tearing mode, whereas the monolithic panels remained intact. Kılıçaslan et al. [18] conducted an experimental and numerical study on the impact response of layered trapezoidal corrugated aluminium core and aluminium sheet interlayer sandwich structures. Here, rate effects were attributed to micro-inertial effects that increased the critical buckling load of the fin at high rates of loading. Radford et al. [19] conducted impact tests on triangular corrugated, pyramidal and aluminium foam core sandwich plates. It was observed that the corrugated and metal foam core sandwich plates offered the best dynamic performance. Tilbrook et al. [20] investigated the dynamic crushing characteristics of sandwich panels based on prismatic lattice cores. Here, the quasi-static and dynamic compression deformation behaviour of stainless steel corrugated and Y-frame sandwich cores were tested. At velocities below 30 m/s, micro-inertial stabilisation against elastic buckling was observed to occur. At higher velocities the propagation of plastic waves within the core resulted in the front face stresses increasing with velocity, whilst the rear surface stresses remained roughly constant. Liang et al. [21] developed lightweight structural concepts for naval applications, with a view to replacing traditional designs with optimised metallic corrugated core sandwich panels. The optimum designs of metallic corrugated core sandwich panels were modelled under blast loading. The authors showed that parameters, such as the corrugation angle and core thickness, are important when designing the core structure.

Recently, Mohr and Marcadet [22] developed a phenomenological ductile fracture initiation model to predict ductile fracture for high strength metallic materials. Here, an extended Mohr–Coulomb criterion is proposed, which makes use of the Hosford equivalent stress in combination with the normal stress acting on the plane of maximum shear. The validation with experimental results indicates that the proposed Hosford–Coulomb model can be used to accurately predict the onset of ductile fracture in advanced high strength steels. Also, Roth and Mohr [23] undertook extensive experimental and numerical work to investigate effect of strain rate on ductile fracture initiation in advanced high strength steel sheets. The extended stress-state dependent Hosford–Coulomb fracture initiation model is proposed to evaluate the strain rate effect on the onset of ductile fracture, which is also successfully validated against the experimental results. These state of the art theories could be used to simulate ductile fracture of metallic materials.

In the present work, a range of metallic curvilinear corrugated-core sandwich structures has been developed [24]. These panels are made in a continuous process by adhesively-bonding two face sheets to a core consisting of a wave-formed aluminium alloy. These panels are finding use in a range of applications in the construction sector, the transport industry and other load-bearing mechanical engineering applications.

The aim of this study is to investigate the dynamic response of such curvilinear corrugated-core sandwich structures, when subjected to low velocity impact loading. The impact response of these structures is subsequently modelled and the resulting models are then used to investigate other loading conditions and material systems.

2. Experimental procedure

The corrugated-core sandwich structures investigated in this study were based on an EN AW-5182 H48 aluminium alloys supplied by Metawell® in Germany [24]. The sandwich panels were manufactured by adhesively bonding two flat alloy skins to a curvilinear alloy core material. Fig. 1 shows the basic design of the sandwich panels investigated here. Two panel configurations, with different face sheet thicknesses and core sizes, were tested, details of which are given in Table 1.

Low velocity impact tests were conducted using an Instron CEAST 9350 falling-weight impact tower. A piezoelectric load sensor was imbedded at the tip of an impactor holder, which makes the impactor replaceable. An impact mass of 5.32 kg, with a 25.4 mm diameter spherical steel head, was used for all tests. Loading data were acquired as voltage output and then transferred into a module 64K DAS (Data Acquisition Station) at a frequency of 100 kHz. Impact velocity was acquired by a photoelectric sensor. During the impact test, the impactor holder was released and dropped vertically passing through the photoelectric sensor beam. At the tip of impactor right at the surface of specimen, the impact velocity was detected. The error of the measured velocity is within 0.01 m/s. Each impact velocity was acquired by a certain height, which was calculated from the required impact energy. The tests were conducted by a varying impact velocity between 1.9 and 5.4 m/s. This range of velocities correlates the strain rate from 100 to 150 s^{-1}. Displacement was calculated by Pro Analyst software, basically considered from load–time relation.

Square test panels, with an edge length of 155 mm, were clamped by a cylindrical ring with inner and outer diameters of 76 and 100 mm, respectively. A clamping force of 200 Newtons was applied

Table 1
Panel dimensions and areal density for the aluminium alloy panels.

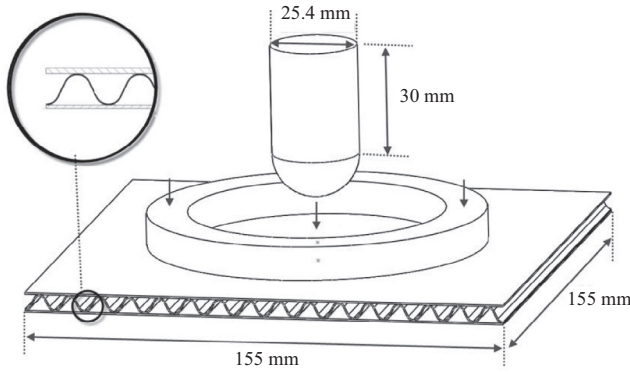| Type	t_1 (mm)	t_w (mm)	t_2 (mm)	H (mm)	D (mm)	Areal density (kg/m^2)
Alu hl/H6	0.5	0.2	0.5	6.0	9.0	3.8
Alu hl/H10	0.8	0.3	0.5	10.0	13.4	5.2

Fig. 2. The experimental test set-up for low velocity impact testing.

to hold the panels in place during testing. Further details of the panel configuration and test conditions are given in Fig. 2. Following impact, the test panels were sectioned through the point of impact and examined under an optical microscope in order to highlight the failure mechanisms that occurred during the impact event.

The mechanical properties of the aluminium alloy were determined by conducting tensile tests on rectangular samples with length and width dimensions 200×25 mm and removed from the skin of an untested panel. The tests were undertaken on an Instron 4505 universal test machine at a crosshead displacement rate of 1 mm/minute, according to ASTM E8/E8M [25]. The data obtained from the tensile tests on the aluminium alloy skins are given in Table 2.

3. Finite element modelling

ABAQUS/Explicit [26] was used to develop numerical simulations of corrugated-core sandwich structures subjected to low velocity impact loading. The aluminium alloy was modelled as an isotropic elasto-plastic material that exhibits rate-dependent behaviour. The total strain rate can be decomposed into an elastic component, $\dot{\varepsilon}^{el}$, and a plastic component, $\dot{\varepsilon}^{pl}$:

$$\dot{\varepsilon} = \dot{\varepsilon}^{el} + \dot{\varepsilon}^{pl} \tag{1}$$

The isotropic rate-dependent material is assumed to obey a uniaxial plastic flow rule and the relationship of the equivalent plastic strain-rate is below:

$$\bar{\varepsilon}^{pl} = h(\bar{\sigma}, \bar{\varepsilon}^{pl}) \tag{2}$$

In which h is a strain hardening function, $\bar{\sigma}$ is the von-Mises equivalent stress, and $\bar{\varepsilon}^{pl}$ is the equivalent plastic strain, which are shown as follows:

$$\dot{\bar{\varepsilon}}^{pl} = \sqrt{\frac{2}{3}\dot{\varepsilon}_{ij}^{pl} : \dot{\varepsilon}_{ij}^{pl}} \text{ and } \bar{\varepsilon}^{pl} = \int_0^t \dot{\bar{\varepsilon}}^{pl} dt \tag{3a}$$

$$\bar{\sigma} = \sqrt{\frac{2}{3}\sigma_{ij}^d : \sigma_{ij}^d}, \sigma_{ij}^d - \text{diviatoric stress} \tag{3b}$$

The isotropic hardening data for the EN AW-5182 H48 aluminium alloy are given in Table 2. The density of the aluminium was

Table 3
Materials properties and parameters for EN AW-5182 H48 aluminium alloy used in finite element modelling.

Property	Value
Young's modulus (GPa)	68
Density (kg/m^3)	2650
Strain rate (s^{-1})	100–150
Fracture strain for ductile damage	0.065
Stress triaxiality	0.33
Fracture energy (kJ/m^2)	67 [28]

taken as $\rho = 2690 \text{ kg/m}^3$. The material properties of this alloy are detailed in Table 3, where the first 4 parameters were determined experimentally and stress triaxiality was estimated based on the tension-shear failure mode [27]. A constant plastic strain-rate was used to cover the range of loading conditions considered when developing the finite element models.

The uniaxial plastic strain, ε_{pl}, which is based on recoverable elastic strain, can be calculated using the following equation:

$$\varepsilon^{pl} = \varepsilon_{total} - \frac{\sigma_{total}}{E} \quad \sigma_{total} > \sigma_y^\circ \tag{4}$$

where σ_{total} is any stress level exceeding the initial yielding point, ε_{total} is the total strain corresponding to σ_{total}, E is modulus of elasticity and σ_y° is the initial yield stress. Furthermore, the constitutive equations with strain hardening employed in the numerical modelling can be expressed as

$$\bar{\sigma} = \begin{cases} \varepsilon^{el} E, & \sigma \leq \sigma_y^\circ \\ 15.65\ln(\bar{\varepsilon}^{pl}) + 278.14, & \sigma > \sigma_y^\circ \end{cases} \tag{5}$$

The rate-dependent hardening curves can be expressed using the following:

$$\bar{\sigma}(\bar{\varepsilon}^{pl}, \dot{\bar{\varepsilon}}^{pl}) = \sigma_y(\bar{\varepsilon}^{pl})R(\dot{\bar{\varepsilon}}^{pl}) \tag{6}$$

In which σ_y is the static yield stress in different hardening stages and R is the stress ratio ($= \bar{\sigma}/\sigma_y$). In the quasi-static case, $R = 1$ at $\dot{\bar{\varepsilon}}^{pl} = 0$ and $\bar{\sigma} = \sigma_y^o$. Another stress ratio is related to the dynamic loading rate, e.g. $R = 1.15$ at $\dot{\bar{\varepsilon}}^{pl} = 100 \text{ s}^{-1}$ and $\bar{\sigma} = \sigma_y$.

The ductile damage criterion is a phenomenological model for predicting the initiation of damage due to nucleation, growth as well as the coalescence of voids. The ductile damage model assumes that the equivalent plastic strain associated with the initiation of damage, $\bar{\varepsilon}_D^{pl}$, depends on the stress triaxiality and equivalent strain-rate [26,29]:

$$\bar{\varepsilon}_D^{pl} = \frac{\bar{\varepsilon}_{bt}^{pl}\sinh\left(k_o\left(-\frac{2}{3}-\eta\right)\right) + \bar{\varepsilon}_{bc}^{pl}\sinh\left(k_o\left(\eta-\frac{2}{3}\right)\right)}{\sinh\left(-\frac{4}{3}k_o\right)} \tag{7}$$

where $\bar{\varepsilon}_{bt}^{pl}$ and $\bar{\varepsilon}_{bc}^{pl}$ are the equivalent plastic strain at ductile damage initiation for equibiaxial tensile and equibiaxial compressive deformation respectively, η is the material stress triaxiality $\left(\eta = -\frac{p}{\bar{\sigma}}\right)$, p is the pressure stress, and k_o is a material constant. The condition for damage initiation is satisfied when:

Table 2
Isotropic hardening data for the EN AW-5182 H48 aluminium alloy.

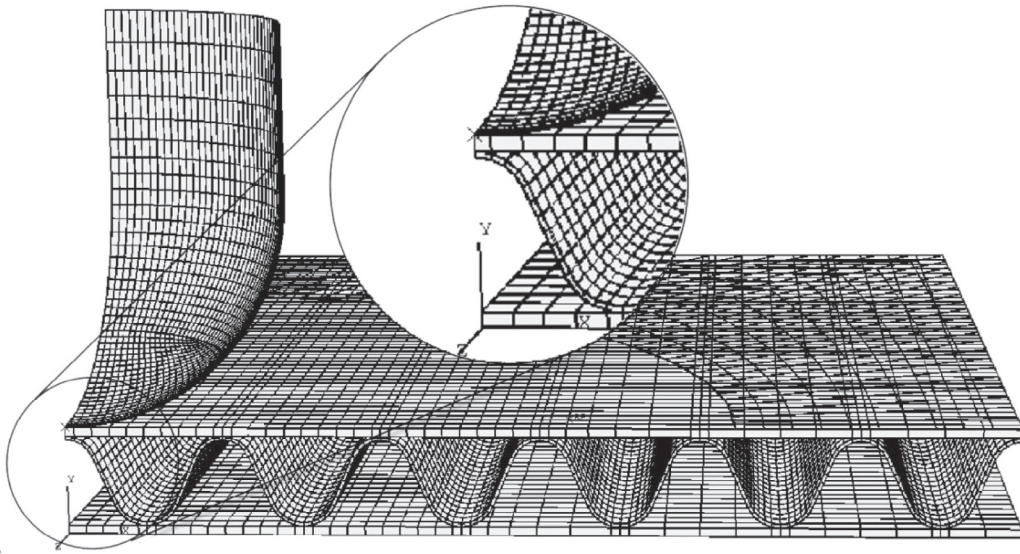| Yield stress (MPa)	153	160	178	203	214	224	231	234	235
Plastic strain	0	0.0004	0.002	0.013	0.020	0.030	0.040	0.050	0.056

Fig. 3. The finite element mesh of a quarter-sized model.

$$\omega_D = \int \frac{d\bar{\varepsilon}^{pl}}{\bar{\varepsilon}_D^{pl}\left(\eta, \dot{\bar{\varepsilon}}^{pl}\right)} = 1 \qquad (8)$$

In which ω_D increases monotonically with increasing plastic deformation. Following each increment in the analysis, the ω_D is computed as:

$$\Delta\omega_D = \frac{\Delta\bar{\varepsilon}^{pl}}{\bar{\varepsilon}_D^{pl}\left(\eta, \dot{\bar{\varepsilon}}^{pl}\right)} \geq 0 \qquad (9)$$

When the ductile failure criterion is satisfied at a given point, all of the stress components are then reduced to zero and it is assumed that the material point is assumed to have failed. If all of the material points at any one section of an element fail, the element is removed.

In order to reduce CPU time, only a quarter of the model, with one element through the sheet thickness, was generated, as shown in Fig. 3. The aluminium corrugated core and skin parts were discretised with a uniform mesh, consisting of 8-noded linear brick elements with reduced integration and hourglass control (C3D8R). The core and skins were fully bonded with a tie constraint at the interface areas, since debonding did not occur during the test. A 4-node 3-D bilinear rigid quadrilateral element (R3D4) was used to mesh the support rings and the spherical projectile. The finite element modelling has been carried out to investigate the influence of the number of elements through the thickness on the impact response. Fig. 4 shows that there is no significant difference on the simulated load–displacement relationships obtained from the models with one, two or three elements through the thickness. Therefore, only one element through the sheet thickness is used in the current study.

The lower support ring was fully fixed, whilst the upper ring was clamped with a force of 200 Newtons to model the experimental clamping condition. The 5.32 kg projectile was constrained to move in the y-direction with a predefined initial velocity.

A surface-to-surface contact interaction was created to allow for sliding between the projectile surface and the individual nodes located in the central region of the target. Also, a general contact interaction was used for self-contact between the inner surfaces of the skins and the individual cells in the core. A friction coefficient of 0.3 was used to represent tangential contact interactions and a hard contact was assumed in the normal direction.

4. Results and discussions

4.1. Experimental results and validation of the numerical model

Fig. 5 shows cross-sections of the 6 mm thick panels following impact at energies between 10 and 80 Joules. Damage at the lowest energy takes the form of buckling within the cells in the central region, as well as permanent plastic deformation in the upper-most skin. Increasing the energy to 20 Joules results in complete crushing of the cells under the impactor and slight deformation of the lower skin. Fracture of the top and bottom layer is in evidence following a 40 Joule impact, with this form of damage becoming more severe as the energy is increased to 50 and then 60 Joules. Finally, the target is fully perforated following an 80 Joule impact, with the projectile passing through the panel. In spite of the severe level of damage, it is interesting to note that this damage remains localised to the point of impact. Indeed, closer inspection of the cross-sections suggests that damage never extends beyond one cell width on either side of the impact zone. This evidence indicates that energy is absorbed over a region immediate to the point of impact.
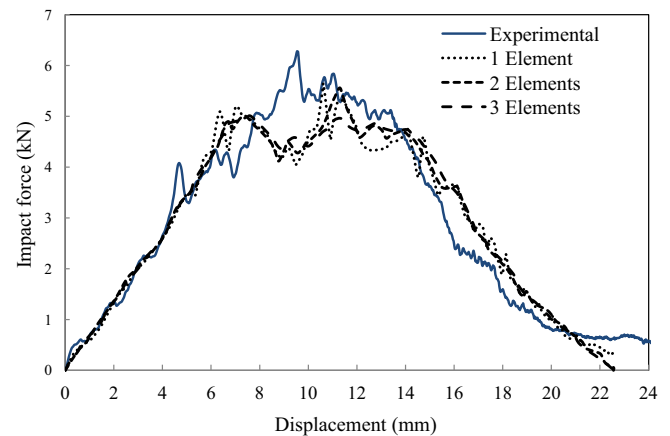

Fig. 4. Comparison of the experimental load–displacement trace and the predicted ones using models with different number of elements through the sheet thickness for an Alu hl/H6 panel subjected to an impact energy of 80J.
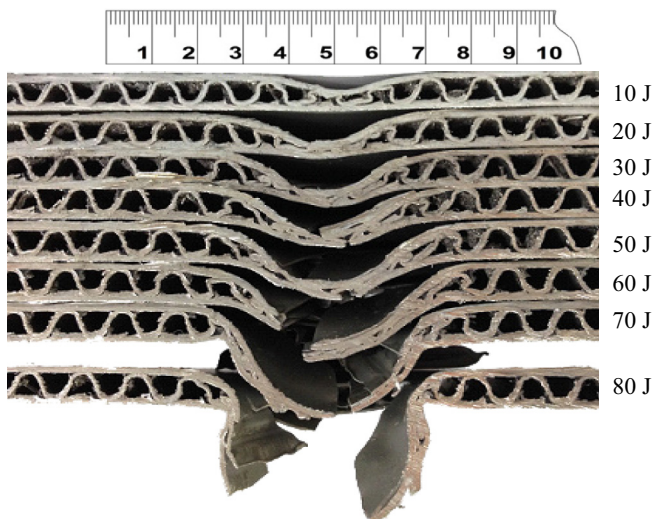
Fig. 5. The progressive damage developed in the 6 mm thick panel.

Fig. 6 shows cross-sections of the 10 mm panels following impact at energies between 15 and 120 Joules. Here, again, initial damage takes the form of buckling of the curvilinear cells under the indentor and plastic deformation of the uppermost skin. Following a 30 Joule impact, the central core region has been completely crushed and the top skin has fractured under the hemispherical impactor. The lower skin was fractured after a 90 Joule impact, where significant localised plastic deformation in outermost skin is evident. Finally, the projectile perforated the panel during a 120 Joule impact, leaving a failure zone in which damage is once again very localised to the point of impact.

Fig. 7 shows typical load–displacement traces following low velocity impact tests on the 6 mm thick panels. Included in each trace is the prediction of the finite element model. At the lowest energy, 20 Joules, the experimental curve increases to an initial peak at 3000 Newtons, at which point the load drops slightly before increasing further via a number of small load drops to 4400 Newtons. Finally, the panel is unloaded as the projectile rebounds, leaving a residual displacement of approximately 6 mm. An examination of the figure indicates that the finite element model captures the principal features of the load–displacement traces. Closer inspection shows that the model does not predict
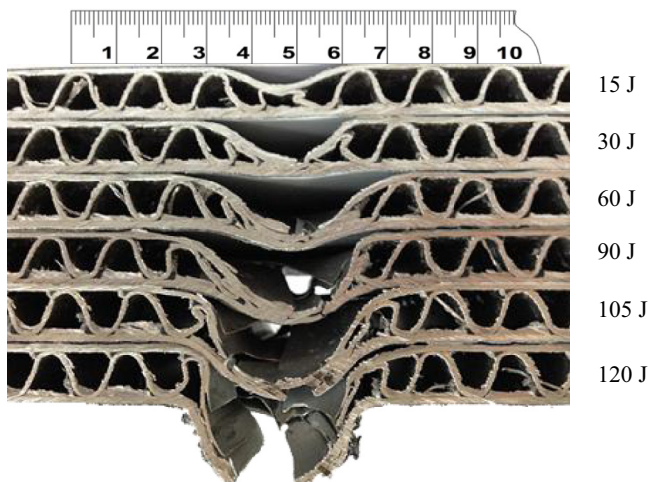

Fig. 6. The progressive damage developed in the 10 mm thick panel.

the small oscillation prior to the maximum in the impact force. Fig. 7(b) shows the corresponding load–displacement traces following a 30 Joule impact. Here, the experimental trace increases to an initial peak of 4200 Newtons, before reaching a maximum at approximately 5000 Newtons. The sudden spike in the load is assumed to be associated with some form of ringing in the load-cell. Again the model predicts the impact response of these thinner panels with reasonable success.

Following the rebounding process, a residual dent of approximately 10 mm is observed in the experimental trace. Increasing the impact energy to 60 Joules results in an enlarged load–displacement trace with significant energy absorption occurring. Here, the experimental trace oscillates around a force of approximately 4500 Newtons, as the projectile penetrates through the panel. Finally, complete perforation of the corrugated sandwich panel occurs when the incident impact energy is increased to 80 Joules. An examination of the two traces in Fig. 7(d) indicates that there is very good agreement between the predicted and measured response. The predicted value of perforation energy, as measured from the area under the load–displacement trace, is approximately 71 Joules, a value that is similar to the experimental value of 75 Joules.

Fig. 8 shows typical load–displacement traces following low velocity impact tests on the 10 mm thick sandwich panels. At the lowest energy of 30 Joules, Fig. 8(a), the experimental load–displacement trace increases in a roughly linear fashion up to a peak at approximately 4400 Newtons before dropping rapidly, prior to increasing to a second peak and subsequent unloading. An examination of the figure indicates that the finite element model accurately predicts the overall response. An examination of the model indicates that the initial drop in load is associated with localised buckling in the curvilinear core. Increasing the incident energy to 60 and then to 90 Joules resulted in a similar trace, although the final peak load is clearly much higher than that at 30 Joules. Finally, the panel is completely perforated following impact at 120 Joules, with the panel absorbing an energy equivalent to approximately 116 Joules, a value that compares favourably with the predicted value of 121 Joules.

The accuracy of the finite element models was assessed by comparing the predicted maximum impact force against the corresponding experimental values and these data are presented in Fig. 9(a). Here, it is clear that the predictions of the FE models are in close agreement with the experimentally-measured values for both the thin and thick sandwich panels. Indeed, the largest error between the two sets of data was approximately 10%. Similar levels of agreement are apparent when the predicted levels of absorbed energy are plotted against the experimental values, Fig. 9(b). Here, the average error between the predicted and measured values of absorbed energy is 7%. The evidence in Fig. 9(a) and (b) supports the conclusion that the finite element model is able to accurately predict the low velocity impact response of these corrugated core sandwich structures.

Fig. 10 shows the numerical predictions of the cross-sections of the 6 mm thick sandwich panels, based on the distribution of the equivalent plastic strain. It was found that the equivalent plastic strain corresponding to the true triaxial stress around the crack tip is much higher than the uniaxial damage initiation strain (Table 3) due to a very high strain concentration there. These cross-sections can be compared to the equivalent experimental cross-sections in Fig. 5. A comparison of the experimental and numerical cross-sections indicates that the finite element model accurately captures the key failure mechanisms occurring within the panels. Here, the high levels of plastic deformation occurring within the upper and lower skins is clearly evident, as well as the localised region of fracture observed in the surface layers. Closer inspection indicates that the zones over which the upper and lower skins are seen to deform is slightly greater in the models than in the actual panels. Apart from this
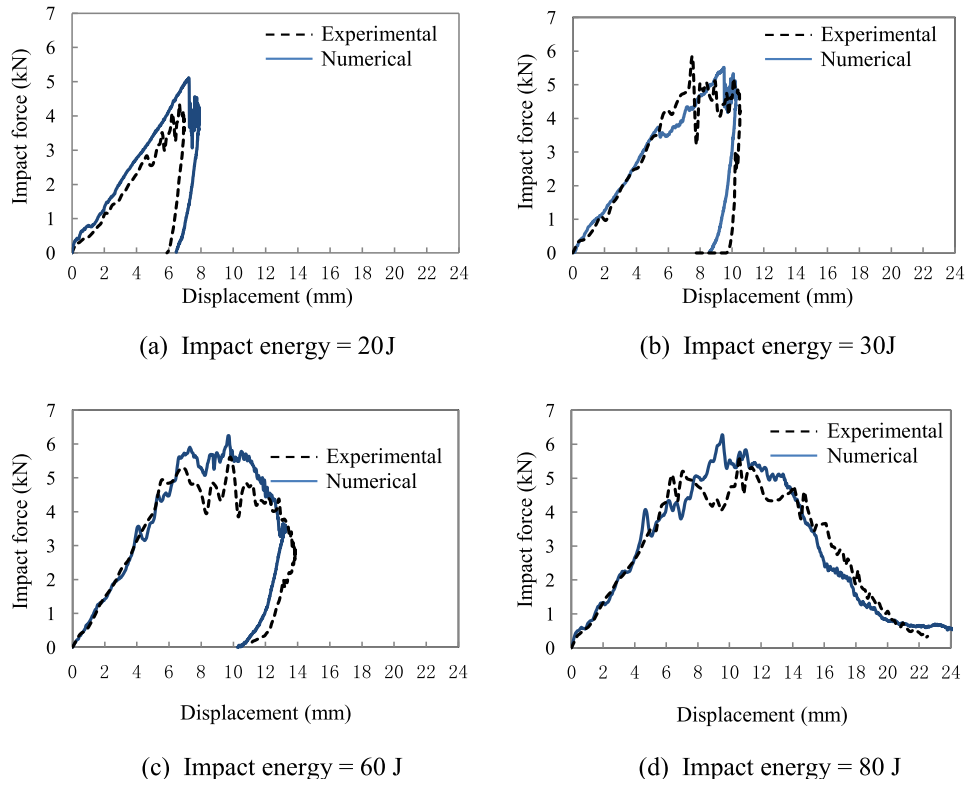
Fig. 7. Load–displacement plots from Alu hl/H6 panels in ascending impact energy. (a) 20 J, (b) 30 J, (c) 60 J, (d) 80 J.

discrepancy, it appears that the model accurately predicts the failure processes in these sandwich panels.

Fig. 11 shows cross-sections of the impact-damaged 10 mm panels, as predicted by the finite element analysis, again based on the distribution of the equivalent plastic strain. At the lowest energy, 15 Joules, the top skin is permanently deformed in the vicinity of the impactor, resulting in localised buckling of the curvilinear web. This is most evident in the central cell, where the walls of the web
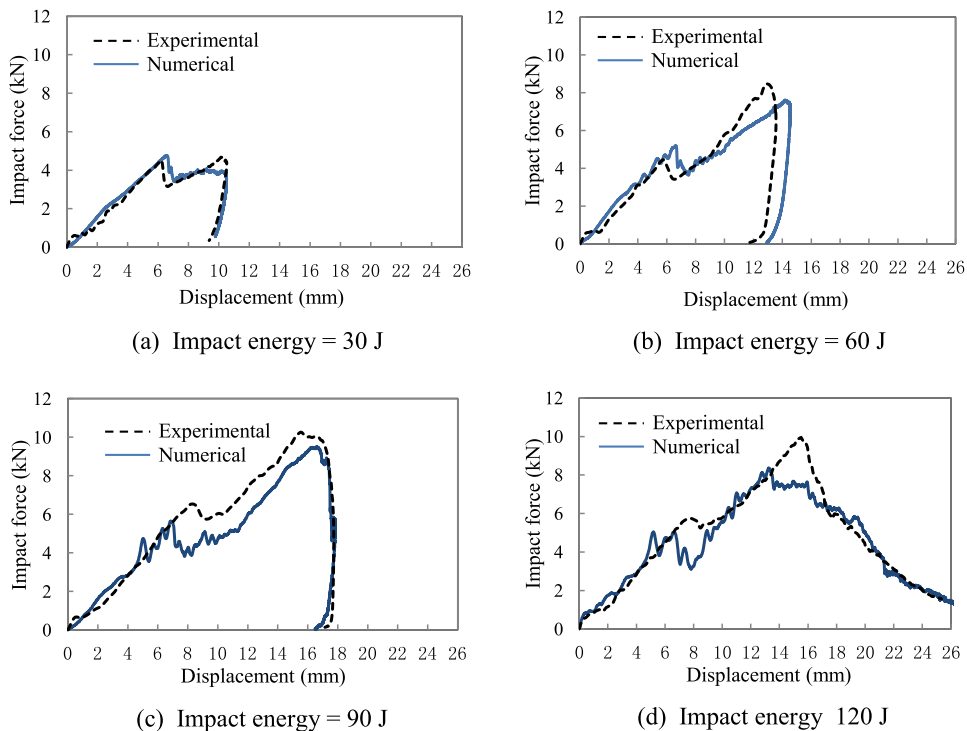
Fig. 8. Load–displacement plots from Alu hl/H10 panels ascending impact energy. (a) 30 J, (b) 60 J, (c) 90 J, (d) 120 J.
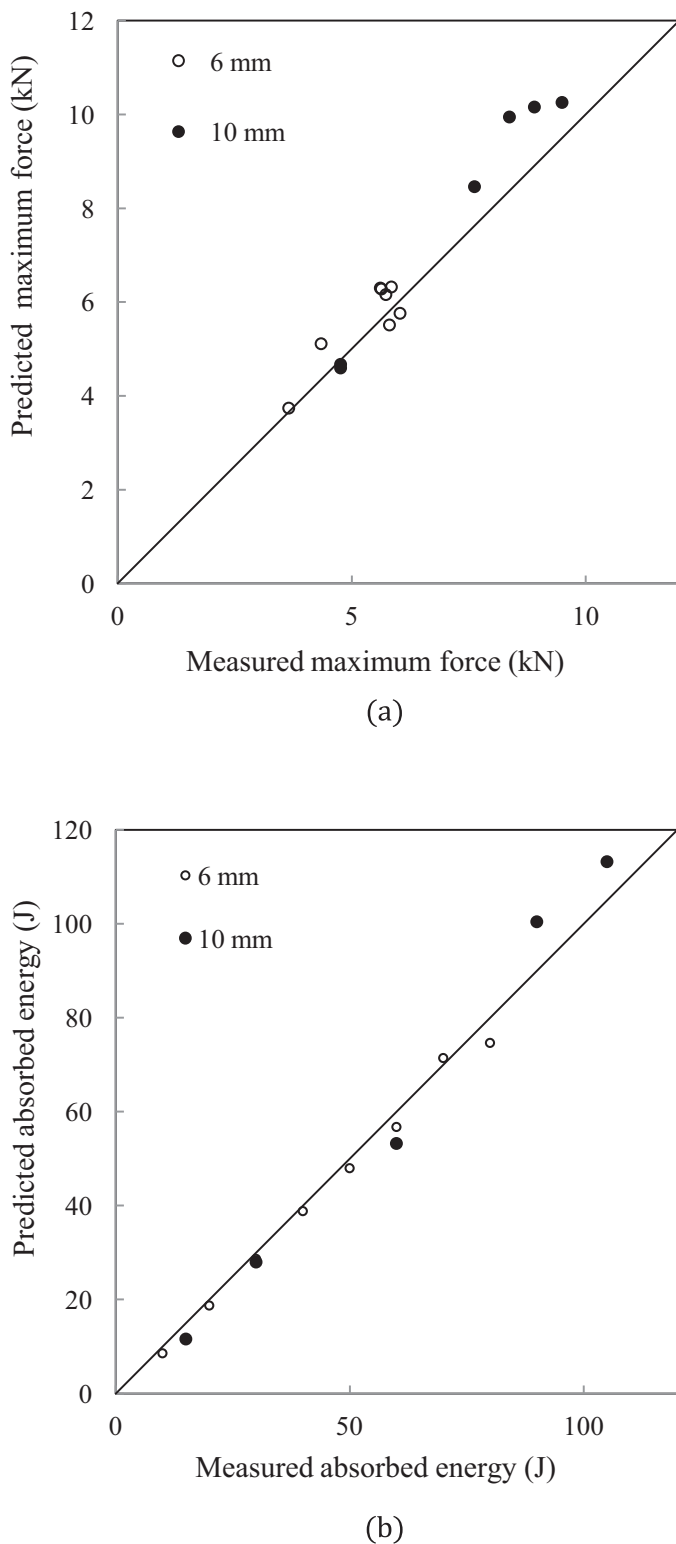
(a)

(b)

Fig. 9. (a) Comparison of predicted versus measured maximum force, (b) Comparison of predicted absorbed energy and measured absorbed energy.

exhibit distinct bulges. Increasing the energy to 30 Joules forces the top skin in contact with the lower skins, effectively crushing the central cell in the process. At an impact energy of 60 Joules, the top face forces the lower skin downwards, a process that continues until the lower skin is clearly fractured following an impact energy of 90 Joules.

This process continues until the panel is fully perforated following a 120 Joule impact. Here, both skins have been highly deformed and the cell immediate to the perforation zone has been damaged. A comparison of these predicted damage patterns with those observed experimentally, Fig. 6, highlights a high level of agreement between the two. The model appears to identify the important failure processes and also predicts that damage remains concentrated over a small volume close to the point of impact.

In the final part of this research investigation, the finite element model was used to understand the influence of varying key parameters on the perforation resistance of these corrugated core sandwich structures. Here, attention focused primarily on investigating the effect of varying the angle at which the projectile strikes the target, the projectile diameter as well as the material properties of the sandwich materials.

4.2. Influence of impact angle on perforation resistance

Typically, it is very difficult to undertake oblique impact tests, particularly using a falling-weight impact rig. This is in part due to the fact that impacts of this nature generate a horizontal force component that drives the impactor against one of the vertical columns used to guide the impactor. One of the advantages of having validated the numerical model is that it can then be used to predict the response of these more complex impact events with reasonable confidence. Fig. 12 shows load–displacement traces generated by the FE analysis for the 6 mm thick panel subjected to impact at angles between 90° (i.e. normal impact) and 50°. It should be noted that the force and displacement are measured along an axis corresponding to the trajectory of the projectile. The initial stiffness of all the panels is similar, with the force rising in a roughly linear fashion up to an initial peak load. The magnitude of this initial maximum in force is similar for all angles, having a value between 4 and 5 kN in all cases. Continued loading results in a second distinct peak, the magnitude of which appears to increase with increasing obliquity. For example, the maximum force predicted for a normal (90°) impact is approximately 5.7 kN, whereas that for a 50° impact is approximately 6.9 kN. The force then reduces to zero, as the projectile perforates the panel. Fig. 13 presents the finite element predictions of the perforated panels following impact at angles between 90° and 50°. All figures again show that damage is localised to the region of impact. It is clear that the length of the distant petal (i.e. that produced as the projectile exits the structure) increases with impact angle. An examination of the impact regions indicates that the formation of this exit petal triggers a localised buckle in the distal layer at higher angles of obliquity.

As before, the area under the load–displacement traces was used to determine the energy required to perforate the panels. Fig. 14 shows the variation of perforation energy with impact angle for the five impact conditions considered for the three materials in this investigation. Here, it is evident that the energy required to perforate the panels increases from 95, 115 and 120 to approximately 148, 195 and 210 Joules for the 2024-T3, the stainless steel and the titanium alloy respectively, as the impact angle is varied from 90° to 50°. This increase in perforation energy is associated with the fact that the projectile has to fracture a larger volume of material as it passes through the target at an off-axis angle. It is also possible that changes in the buckling and collapse response of the cores and the skins lead to a small increase in energy absorption.

4.3. The influence of material properties on perforation resistance

Clearly, the low velocity impact response of the corrugated sandwich structure studied here is likely to be strongly dependent on the type of material from which the cores and the skin are manufactured. In order to investigate this in more detail, finite element
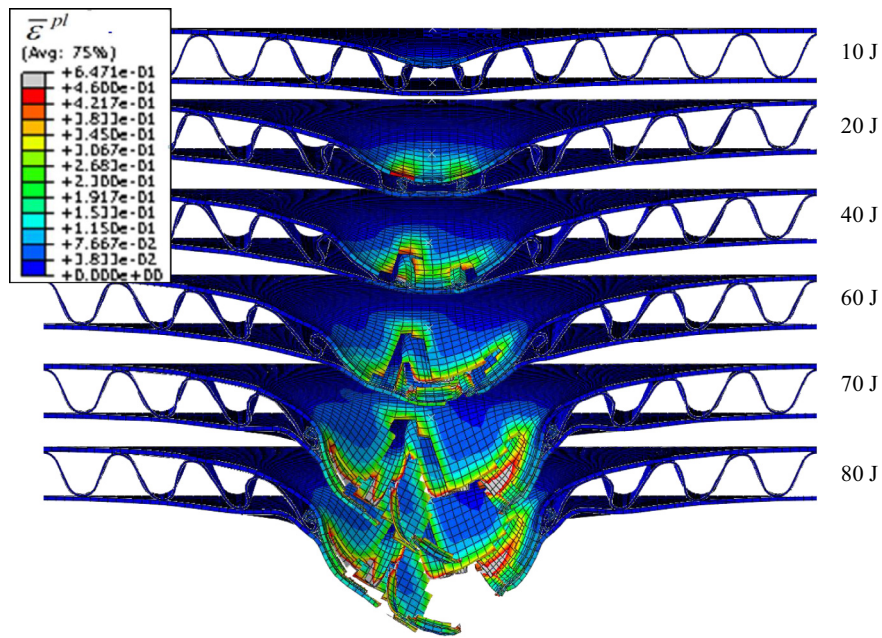
Fig. 10. Finite element predictions of the damage characteristics in the 6 mm thick Al hl/H6 panels.

models were created based on five additional metallic substrates, these being a 2024-T3 aluminium alloy, an A5052 aluminium alloy, a 6061-T4 aluminium alloy, a stainless steel (X5CrNi18-10) [30] and a Ti6Al4V titanium alloy [31]. The mesh and boundary conditions were selected to be the same as those discussed previously and outlined in Figs. 2 and 3. In each case, the response of the panels at the perforation threshold was examined and the energy required to perforate each structure was determined from the load–displacement trace. Fig. 15(a) shows the predicted perforation load–displacement traces for the four aluminium alloys.

An examination of the figure indicates that the 2024-T3 exhibits the highest maximum force, a value associated with the superior yield strength and tensile strength of this alloy. In contrast, the A5052

alloy offers a reduced response, linked to the poorer mechanical properties of this alloy. The model also predicts that this alloy undergoes a greater displacement during the impact event. Fig. 15(b) compares the load–displacement responses of the titanium and stainless steel-based sandwich structures with the 2024-T3 alloy. Clearly, there is some similarity in all three traces, with the titanium alloy exhibiting the higher impact forces throughout the event.

Fig. 16 summarises the predicted perforation resistances of the four aluminium alloy sandwich structures, as well as those of the stainless steel and the titanium alloy. An examination of the figure indicates that the 2024-T3 alloy offers the highest perforation energy of the four aluminium alloys. The predicted perforation energy for
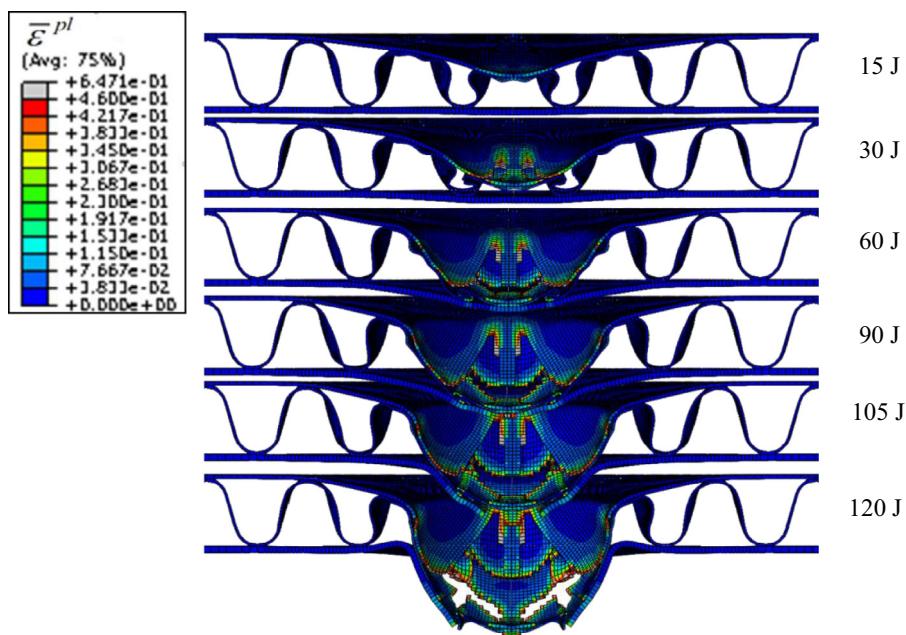

Fig. 11. Finite element predictions of the damage characteristics in the 10 mm thick Al hl/H10 panels.
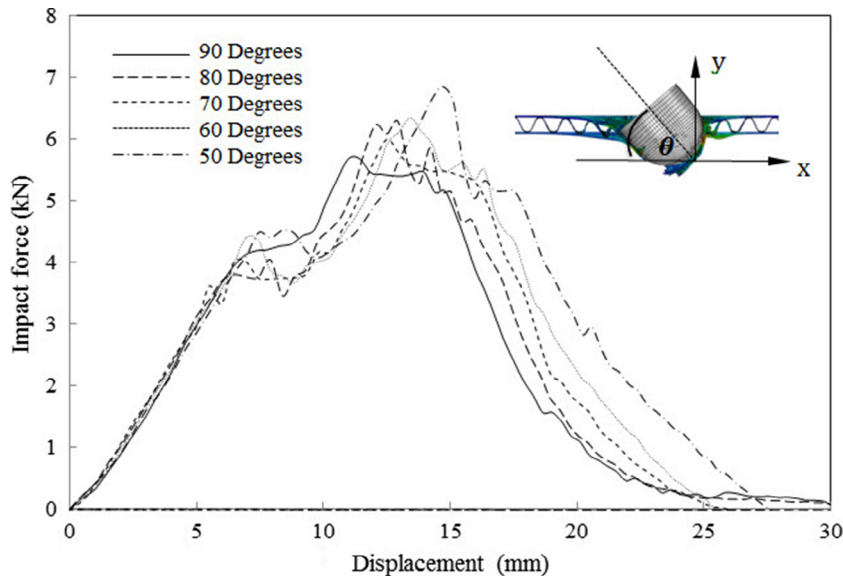
Fig. 12. The influence of angle of obliquity on the perforation resistance of the 6 mm thick sandwich panels.

this alloy is approximately 45% above that of the A5052 system. Clearly, the stainless steel offers a superior perforation resistance to that of the aluminium alloys and the titanium alloy offers the highest values of perforation energy, with a value approaching 120 Joules. The perforation energies were divided by the areal density of the panels to yield specific values, and these data are included in Fig. 16. Here, it is clear that the 2024-T3 alloy offers the highest specific perforation energy (SPE) of the six material systems con-
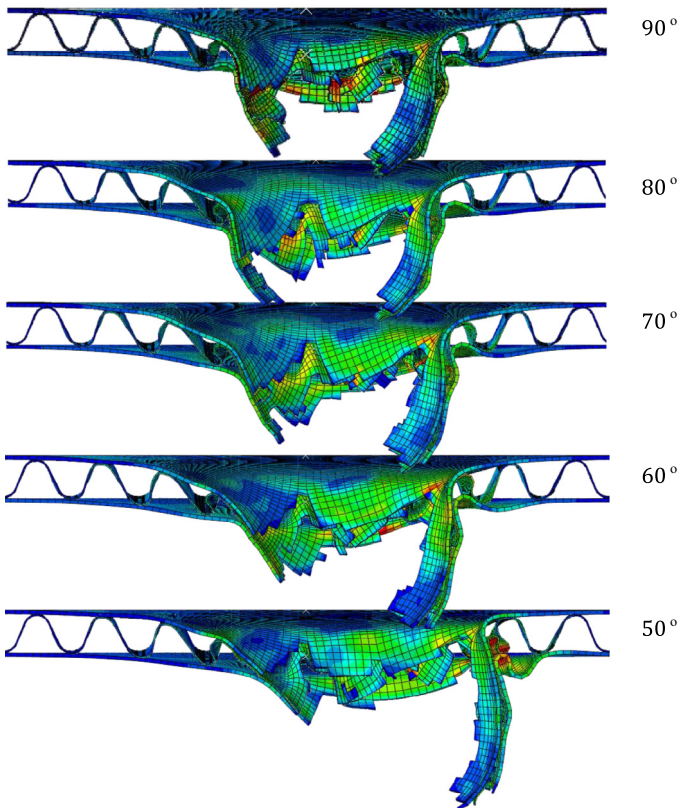
sidered here. Clearly, the higher densities of the stainless steel and titanium alloy greatly reduce the relative perforation resistances of these sandwich structures, with the SPE of the steel and titanium panels being only 33% and 58% that of the 2024-T3 alloy.

4.4. The influence of projectile diameter

The final parameter to be investigated in this study was the projectile diameter. Here, the projectile diameter was varied between 5 and 30 mm. In each case, it was assumed that the projectile impinged the target directly above the apex of the curvilinear. Three material systems were investigated, these being stainless steel, titanium alloy and the 2024-T3 alloy. Fig. 17 shows the variation of perforation energy with projectile diameter for the three material systems. As expected, the perforation energy is predicted to increase with projectile diameter. The predicted increase is non-linear. For example, the energy required to perforate the 2024-T3 panel with a 5 mm diameter impactor is predicted to be 10.3 Joules, whereas that for the 30 diameter impactor is 130 Joules. As before,
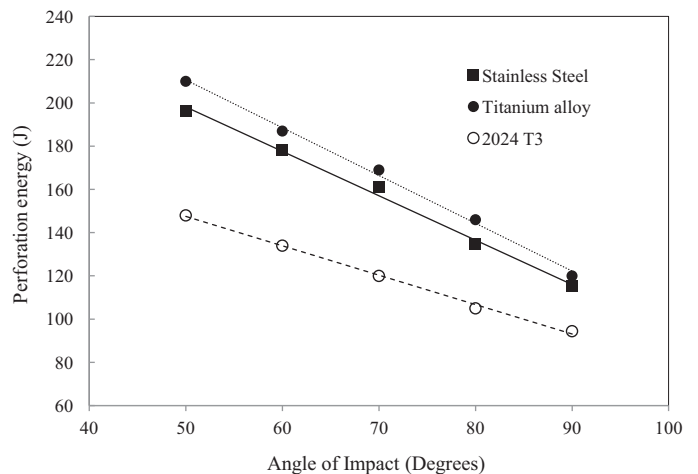

Fig. 13. Finite element predictions of damage at the perforation threshold in 6 mm thick panels impacted at angles between 90° (normal) and 50°.

Fig. 14. The validation of perforation energy with angle of obliquely for the 2024-T3 aluminium alloy, the stainless steel and the titanium alloy.
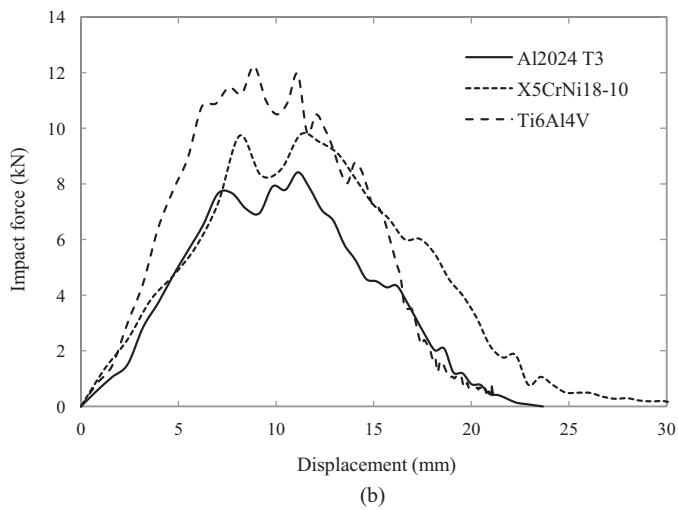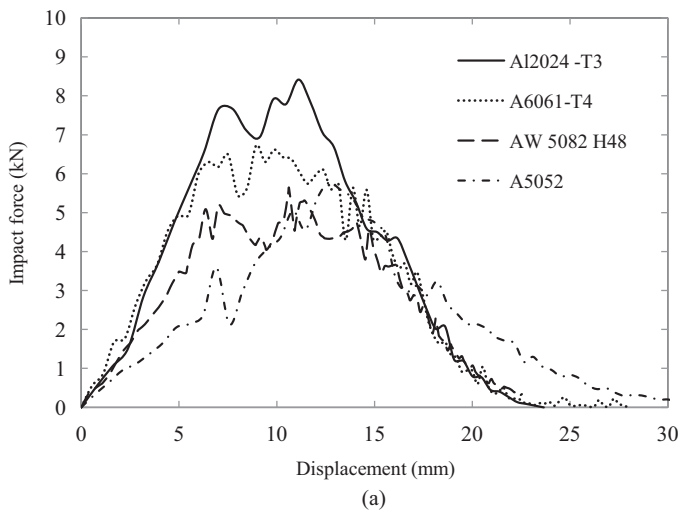
(a)
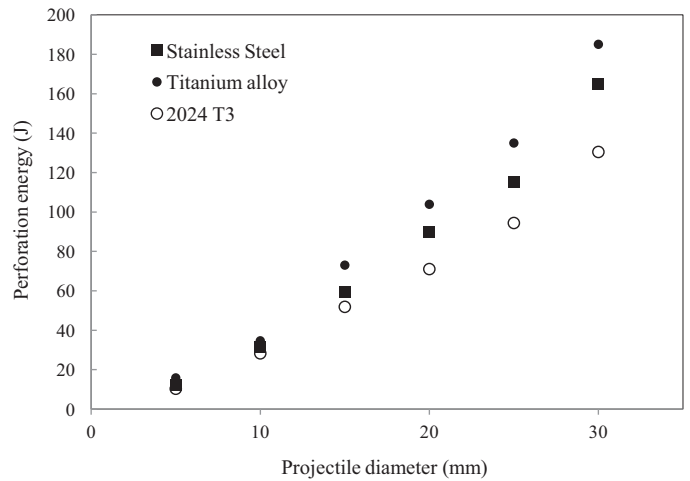
Fig. 17. The variation of perforation energy with projectile diameter for three sandwich structures.

the titanium alloy offers the most impressive performance; however, this is at the expense of an increased panel weight.

5. Conclusions

The low velocity impact response of all-metal sandwich panels based on a curvilinear core has been investigated both experimentally and numerically. Initially, the attention focused on understanding the experimental response of two thicknesses of an all-aluminium sandwich structure. Here, at low energies, failure took the form of a top surface dent, stretching of the upper skin and buckling of the core structure. Higher impact energies resulted in fracture of the skins and core, fracture mechanisms that were localised to the point of impact. The low velocity impact responses of the curvilinear panels were subsequently modelled using finite element analysis techniques. Here, agreement between the measured and predicted load–displacement traces was good at all energy levels. An examination of the damage predicted by the FE analysis indicated that the models accurately captured all of the key failure mechanisms.

Following validation, the FE analysis was used to predict the effect of varying the projectile diameter and the angle of obliquity on the perforation resistance of sandwich panels based on a number of aluminium alloys, as well as a stainless steel and a titanium alloy. Here, it was shown that the perforation energy increases with impact angle, due to the increased volume of material fractured at higher impact angles. Similarly, it has been shown that increasing the projectile diameter serves to increase the perforation energy, with a 2024-T3 aluminium alloy offering the highest specific perforation energy of the six alloys considered here.

References

[1] Biancolini ME. Evaluation of equivalent stiffness properties of corrugated board. Compos Struct 2005;69:322–8.
[2] Nyman U, Gustafsson PJ. Material and structural failure criterion of corrugated board facings. Compos Struct 2000;50:79–83.
[3] Rejab MRM, Cantwell WJ. The mechanical behaviour of corrugated-core sandwich panels. Compos Part B Eng 2013;47:267–77.

(b)

Fig. 15. The predicted load–displacement traces of (a) the four aluminium alloys, (b) comparison of the stainless steel and titanium alloy with the 2024-T3 aluminium alloy.
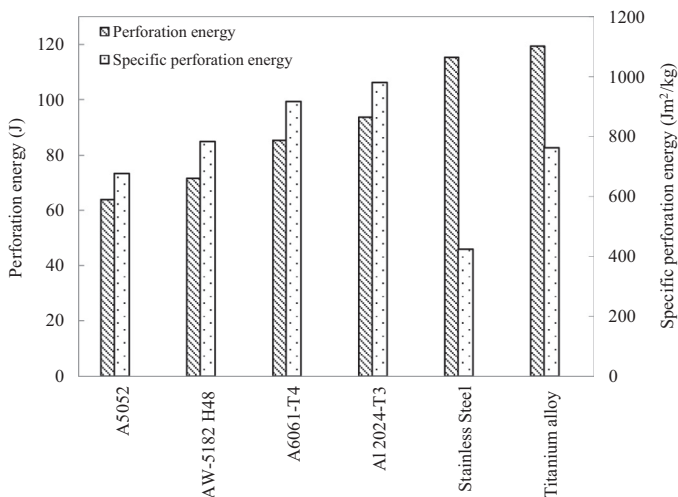

Fig. 16. Summary of the predicted perforation energies and specific perforation energies for the six sandwich structures.

[4] Herrmann A, Zahlen P, Zuardy I. Sandwich structures technology in commercial aviation. In: Thomsen OT, Bozhevolnaya E, Lyckegaard A, editors. Sandwich structures 7: advancing with sandwich structures and materials. Stade, Germany, Springer Netherlands; 2005. p. 13–26.

[5] Kazemahvazi S, Zenkert D. Corrugated all-composite sandwich structures. Part 1: modeling. Compos Sci Technol 2009;69:913–19.

[6] Xiong J, Ma L, Wu L, Liu J, Vaziri A. Mechanical behavior and failure of composite pyramidal truss core sandwich columns. Compos Part B Eng 2011;42:938–45.

[7] Lin Y-K, Liu H-K, Kuo W-S, Chen Y-D. Fracture evolution in thick composites under compression. Polym Compos 2007;28:425–36.

[8] Zenkert D. An introduction to sandwich construction, Stockholm, Sweden, Engineering Materials Advisory Services Ltd, 1995.

[9] Zhang ZS, Wang Z. Crush behavior of corrugated cores sandwich panels. Adv Mat Res 2011;217–218:1584–9.

[10] Yokozeki T, Takeda S, Ogasawara T, Ishikawa T. Mechanical properties of corrugated composites for candidate materials of flexible wing structures. Compos Part A Appl Sci Manuf 2006;37:1578–86.

[11] Talbi N, Batti A, Ayad R, Guo YQ. An analytical homogenization model for finite element modelling of corrugated cardboard. Compos Sci Technol 2009;69:913–19.

[12] McKee RC, Gander JW, Wachuta JR. Compression strength formula for corrugated boxes. Paperboard Packaging 1963;48:149–59.

[13] Allaoui S, Aboura Z, Benzeggagh ML. Effects of the environmental conditions on the mechanical behaviour of the corrugated cardboard. Compos Sci Technol 2009;69:104–10.

[14] Isaksson P, Gradin P. Shear buckling in the core of a corrugated board structure. Compos Struct 2009;88:610–14.

[15] Tian YS, Lu TJ. Optimal design of compression corrugated panels. Thin-Walled Structures 2005;43:477–98.

[16] Haj-Ali R, Choi J, Wei B-S, Popil R, Schaepe M. Refined nonlinear finite element models for corrugated fiberboards. Compos Struct 2009;87:321–33.

[17] Rubino V, Deshpande VS, Fleck NA. The dynamic response of end-clamped sandwich beams with a Y-frame or corrugated core. Int J Impact Eng 2008;35:829–44.

[18] Kılıçaslan C, Güden M, Odacı İK, Taşdemirci A. The impact responses and the finite element modeling of layered trapezoidal corrugated aluminum core

and aluminum sheet interlayer sandwich structures. Mater Design 2013;46:121–33.

[19] Radford DD, Fleck NA, Deshpande VS. The response of clamped sandwich beams subjected to shock loading. Int J Impact Eng 2006;32:968–87.

[20] Tilbrook MT, Radford DD, Deshpande VS, Fleck NA. Dynamic crushing of sandwich panels with prismatic lattice cores Dynamic crushing of sandwich panels with prismatic lattice cores. Int J Solids Struct 2007;44:6101–23.

[21] Liang C-C, Yang M-F, Wu P-W. Optimum design of metallic corrugated core sandwich panels subjected to blast loads. Ocean Eng 2001;28:825–61.

[22] Mohr D, Marcadet J. Micromechanically-motivated phenomenological Hosford–Coulomb model for predicting ductile fracture initiation at low stress triaxialities. Int J Solids Struct 2015;67–68:40–55.

[23] Roth C, Mohr D. Effect of strain rate on ductile fracture initiation in advanced high strength steel sheets: experiments and modeling. Int J Plast 2014;56:19–44.

[24] Metawell. Metal sandwich technology. <http://www.metawell.de/en/metawell-aluminium-sandwich-panels-and-lightweight-components> [Accessed 10.11.15].

[25] ASTM E8/E8M-13a. Standard test methods for tensile testing of metallic materials. West Conshohocken, PA: ASTM international; 2013.

[26] Abaqus 6.12-3. Analysis user's manual. Warrington, Cheshire, Dassault Systemes Simulia Corp.; 2012.

[27] Prantl A, Ruzicka J, Spaniel M, Moravec M, Dzugan J, Konopík P. Identification of ductile damage parameters, 2013 SIMULIA Community Conference, Vienna, Austria, 21–24 May 2013.

[28] Kaufman JG. Fracture resistance of aluminum alloys: notch toughness, tear resistance, and fracture toughness. Prague, ASM International; 2001. p. 60.

[29] Hooputra H, Gese H, Dell H, Werner H. A comprehensive failure model for crashworthiness simulation of aluminium extrusions. Int J Crashworth 2004;9:449–64.

[30] Ozgowicz W, Kalinowska-Ozgowicz E, Kurc A. Influence of plastic deformation on structure and mechanical properties of stainless steel type X5CrNi18-10. J Achiev Mater Manuf Eng 2008;32:37–40.

[31] Lesuer DR. Experimental investigation of material models for Ti-6Al-4V Titanium and 2024-T3, FAA Report, DOT/FAA/AR-00/25, Lawrence Livermore National Laboratory, U.S. Department of Energy, pp.5–13, 2000.